NUMI note 1687
Version 1.0
March 28, 2006

Analysis of the Atmospheric Muon Charge Ratio with the MINOS Underground Far Detector

T. Fields, G. Giurgiu[1], M. Goodman, J. Reichenbacher, P. Schreiner

Argonne National Laboratory

Abstract

We present a study of the atmospheric muon charge ratio using the underground MINOS far detector. Data were collected between July 2003 and April 2005. The magnetic field of the detector was in forward configuration for about two thirds of the time and in reverse field configuration for one third of the time. After combining the forward and reverse data sets the measured charge ratio for muons with momenta between 0 and 250 GeV is $1.378 \pm 0.004(stat.) \pm 0.009(syst.)$.

[1]to whom comments should be addressed: giurgiu@anl.gov

1 Introduction

In this note we present a measurement of the cosmic muon charge ratio using the MINOS far detector. Cosmic ray muons are produced when primary nuclei, mostly protons, hit nuclei at the top of the atmosphere. Since the protons and the air nuclei are positively charged, there are more positive particles, primarily pions produced in the hadronic showers resulting from proton-nucleus collisions. These pions decay into the observed cosmic ray muons which are detected underground by the MINOS far detector. The muon energy loss in the atmosphere is of the order of GeV, while the subsequent energy loss through the rock is of the order of TeV.

The purpose of this analysis is two-fold. First, it provides a precise measurement of the muon charge ratio (N_{μ^+}/N_{μ^-}) which can be useful in constraining theoretical models of the atmospheric neutrino flux. The muon energy measured underground could be extrapolated to the surface to provide a measurement of the charge ratio in the TeV range which has not been explored at that accuracy before. Secondly, this is a calibration measurement demonstrating the charge identification capabilities of the MINOS far detector. Muon charge identification is essential for separating neutrinos from anti-neutrinos.

2 Data Set and Event Selection

For this analysis we use data collected with the MINOS far detector between July 2003 and April 2005. During this data taking period the magnetic field in the far detector was in normal configuration for 457 days and in reverse field configuration for 171 days. We analyze a total of about 20,586,613 events out of which 13,055,035 events correspond to the normal field and 7,531,578 events correspond to reverse magnetic field data taking. The data set was reconstructed with version R1.14 of the MINOS reconstruction software.

We start the analysis by selecting events according to a set of basic cuts similar to the ones described and motivated in References [1], [2] and [3]. We remove the following runs/events:

- runs in which the single muon rate is is different by more than 3 σ from the mean of all run rates in the data sample. Here σ is defined as the width of the Gaussian fit to the run rate distribution.
- events containing more than one muon track.
- events for which the demultiplexing algorithm fails.
- tracks for which the plane, digit or strip usage is larger than 1. Here the plane/digit/strip usage is defined as the plane/digit/strip of the track divided by the total plane/digit/strip of the event.
- upward going tracks: $\theta_{zenith} > 89°$
- tracks with length less that 2 meters.
- tracks containing hits in less than 20 planes.

- tracks that fail the track fitting algorithm and tracks with reduced χ^2 larger than 2.0.
- tracks with UV asymmetry A_{UV} larger than 0.11. The UV asymmetry is defined as $2\frac{N_U - N_V}{N_U + N_V}$, where N_U and N_V are the numbers of U and V hits, respectively.
- tracks for which the vertex or the end point are more than 0.5 m outside the detector fiducial volume.
- tracks that are shorter than 4 meters and have less than 60 planes and at the same time the pulse-height usage or the plane usage are less than 0.4.
- tracks for which $(q/p)/\sigma_{q/p} < 2.5$, where q and p are the reconstructed charge and momentum of the muon track (charge significance cut).
- tracks which appear to stop inside the detector volume. A track is considered to be a "stopper" if the endpoint of the track is inside more than 0.5 m from the surface of the detector or more than 2 planes from the extreme planes of each super-module.

Table 1 shows a summary of the initial basic cuts and the number of events left after each cut.

Requirement	Events	Fraction left (%)
no cuts	20586613	100.0
good runs	19859341	96.5
remove multiple muon events	19352116	94.0
remove demultiplexing failures	19330600	93.9
plane/digit/strip usage < 1	18703043	90.9
remove upward going	18564337	90.2
track length $> 2\ m$	17626725	85.6
plane number > 20	14136952	68.7
fit pass and $\chi^2 < 2.0$	13221016	64.2
UV asymmetry cut	12585877	61.1
fiducial cut	12551903	61.0
pulse-height and plane usage < 0.4	12537764	60.9
$(q/p)/\sigma_{q/p} > 2.5$	3442523	16.7
remove stoppers	3310741	16.1

Table 1: Summary of event selection criteria and the numbers of events after each cut.

3 Charge Ratio with the Initial Event Selection

Using the data sample selected according to the cuts described in the previous section, we analyze the muon charge ratio as a function of the track measured momentum and direction.

Figure 1 shows the momentum distribution separately for positive and negative muons corresponding to the forward field data. The median measured momentum of the muons

detected by the underground far detector is ≈ 20 GeV and the tail extends above 250 GeV. The measured momentum becomes quite inaccurate above ≈ 100 GeV since tracks with high momenta are almost straight and the smaller the curvature the more difficult the measurement. The energies of these muons are greatly reduced as compared to their initial energies at the surface due to energy loss through the ≈ 720 m of rock. The surface energy is estimated (see Section 9) to be of the order of 1 TeV. By dividing the momentum distribution histograms for positive and negative muons bin by bin, we obtain the distribution of the muon charge ratio as a function of momentum. A priori we expect these distributions to be flat or to have very slight momentum dependence at most. Figure 1 displays the charge ratio versus momentum for both forward and reverse data sets. Surprisingly, these distributions exhibit unexpected structures around ≈ 40 GeV.

We proceed by studying the charge ratio as a function of the muon direction. In the coordinate system of the detector, we define the following spherical angles: ϕ as the angle between the projection of the muon track in the XY plane and the X axis and θ as the angle between the muon track and the Z axis of the detector. In Figure 2 we show the distributions of the angle ϕ for positive and negative muons for both forward and reverse data sets. It is clear that the ϕ distributions are not symmetric with respect to the vertical plane ($\phi = 90°$). Moreover, the biases seem to be in opposite directions for positive and negative tracks and they reverse with the magnetic field reversal. As there is no physical reason for such effects in the true momentum distribution, we conclude that they are measurement biases. We believe that these biases are due to misalignments within the detector, but other effects, such as magnetic field map errors may also contribute. In a misaligned detector the curvature of a track is distorted and in consequence, its measured momentum could be biased. Also, since the charge of the track is directly measured from its curvature, a false contribution could result in a faulty charge determination. Figure 2 also shows the charge ratio as a function of ϕ for both forward and reverse data sets. The sinusoidal structure of these distributions could be explained by a bias in the measured charge if this bias is ϕ dependent.

In Figure 3 we show the charge ratio as a function of the cosine of the angle θ but also as function of the cosmic azimuth and zenith angles. The gaps in these distributions are due to the requirement that each track passes through at least 20 planes of the detector. Detailed explanations of these gaps are described in References [1], [2] and [3]. We note that at the edges of each gap, the charge ratio has extreme rises or drops. These effects can be easily understood by realizing how the angular distributions are affected by the 20 plane requirement (see References [4]). For example, in the case of the $cos(\theta)$ distribution, the 20 plane cut is correlated with a cut on the angle θ. Horizontal tracks will always pass through 20 plane while vertical ones will only pass through a few planes. A track which passes through the central axis of the detector must satisfy: $\theta < arctan(\frac{800cm}{20\times 6cm}) \approx 81.5°$ which is equivalent to $cos(\theta) > 0.15$, which in turn is about the size of the gap in the $cos(\theta)$ distribution. The spikes in the $cos(\theta)$ distribution are explained as follows. The muon tracks are not straight lines, but they are bent by the magnetic field of the detector. Positive tracks with $\theta \approx 81.5$ which are just at the limit of passing the 20 plane cut and going North ($cos(\theta) > 0$) are bent by the magnetic field in such a way that they will barely pass the cut. On the other hand, negative tracks with same angle will be bent so that they just fail the cut. The net effect is that positive tracks are greatly enhanced and negative one are suppressed around $cos(\theta) \approx 0.15$. Similar scenarios explain the gaps in the azimuth and zenith angle

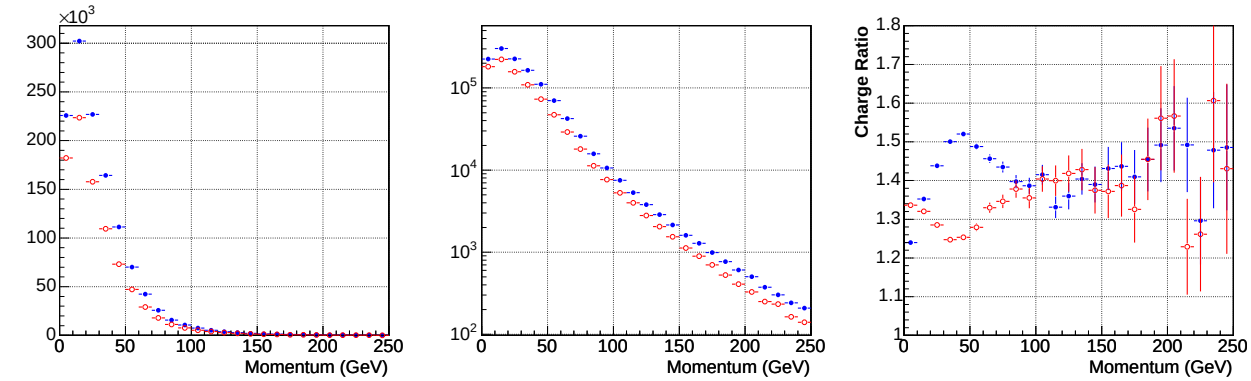

Figure 1: Distributions of measured momentum for positive (full circles) and negative (open circles) muons on both linear (left) and logarithmic (middle) scales for forward field data. The muon charge ratio as a function of muon measured momentum for both forward (full circles) and reverse (open circles) data sets is also shown (right).

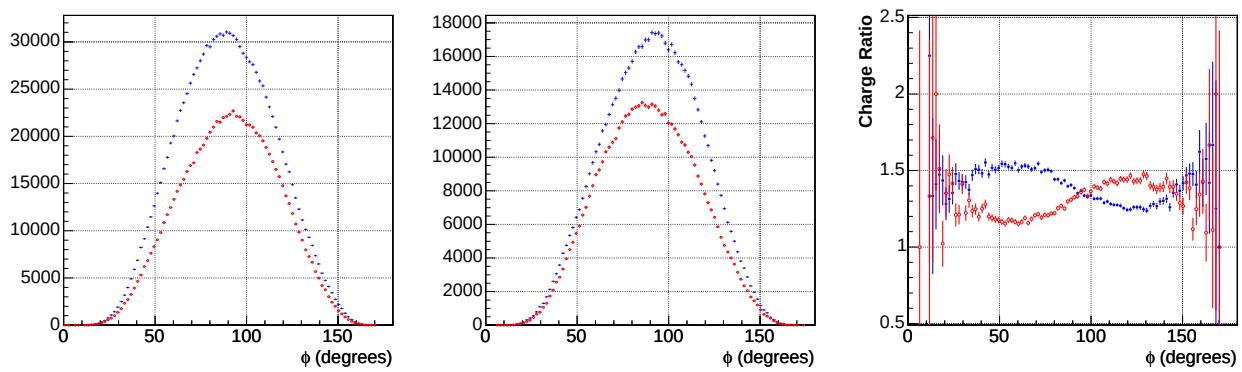

Figure 2: Distributions of the ϕ angle for positive (full circles) and negative (open circles) muons corresponding to the forward (left) and reverse (middle) data. The muon charge ratio as a function ϕ for both forward (full circles) and reverse (open circles) data sets is also shown (right).

distributions.

Besides the well understood gaps and spikes, these angular distributions exhibit structures which are not fully understood, specially the different levels in the plateaus of different B field configurations. We believe that these features are due to direction dependent charge reconstruction biases originating from detector misalignment.

4 Combining the Forward and Reverse Data Sets

In the previous section we determined the muon charge ratio as a function of several quantities for forward and reverse field configurations separately. Having two measurements of the same quantity in different experimental settings, the question is how to combine the two measurements in a single one. This question was addressed in Reference [5] where it

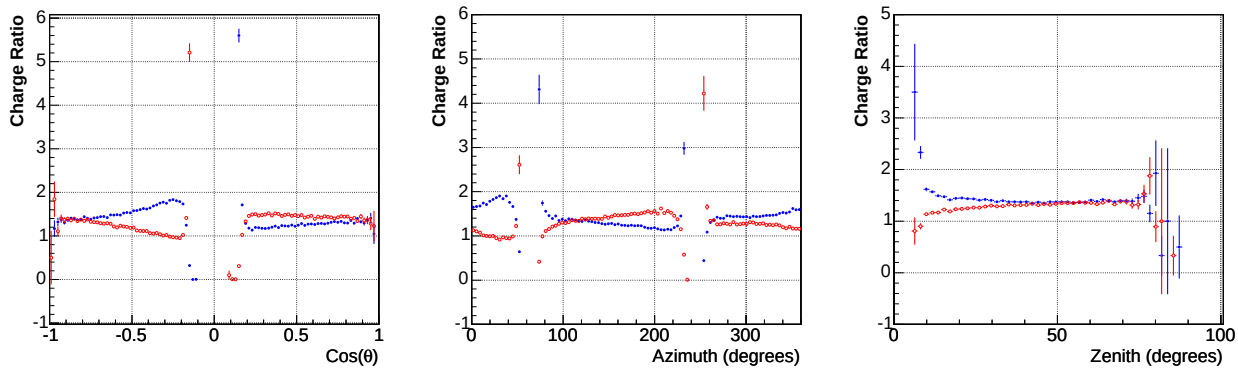

Figure 3: Distributions of the charge ratio versus $cos(\theta)$ (left), azimuth (middle) and zenith (right) angles for both forward (full circles) and reverse (open circles) data sets.

has been demonstrated that having measured the charge ratio in both forward field R_F and reverse field R_R data sets, the true charge ratio R can be calculated as:

$$R = \sqrt{R_F \times R_R}. \tag{1}$$

Following this procedure we calculate the combined charge ratio as a function of momentum, ϕ, $cos(\theta)$, zenith and azimuth angles. The charge ratio is calculated in each bin using Equation (2) $R^i = \sqrt{R^i_F \times R^i_R}$, where i runs over the bins in a given quantity. The error in each bin is given by:

$$\sigma_{R^i} = \frac{1}{2}\sqrt{\frac{R^i_R}{R^i_F}\sigma^2_{R^i_F} + \frac{R^i_F}{R^i_R}\sigma^2_{R^i_R}}, \tag{2}$$

where $\sigma_{R^i_{F/R}}$ is the error on the charge ratio in bin i.

Figures 4 and 5 show the distributions of the charge ratio as a function of momentum, ϕ, $cos(\theta)$, azimuth and zenith after combining the forward and reverse data sets. All four angular distributions become flat and the structure in the momentum distribution around ≈ 40 GeV is removed. This is what we expect to happen if the removed structures are due to curvature biases from misalignment of the detector or magnetic field map errors. Detailed discussions of the curvature biases (from detector misalignment) on the charge ratio versus momentum distributions can be found in References [5] and [6] where it is shown that small biases in the measured curvature of a track can produce structures in the charge ratio versus momentum distributions similar to the ones in Figure 1. It is shown in the same References that combining the forward and reverse data sets according to Equation (2) will remove the structures.

As seen in Figure 4, the charge ratio versus momentum distribution, although has less structure than for either forward or reverse cases, it is still not flat after combining the forward and reverse data sets. The charge ratio drops substantially for low momentum tracks. This was again an unexpected effect since the momentum and the charge of a track should be better measured at low momentum where the curvature of the track is large.

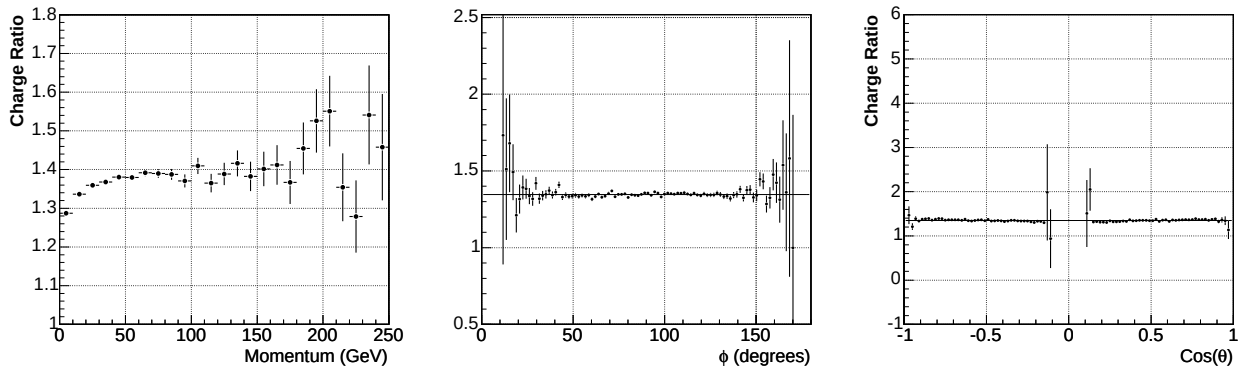

Figure 4: Charge ratio as a function of momentum, ϕ and $cos(\theta)$ after combining the forward and reverse data sets.

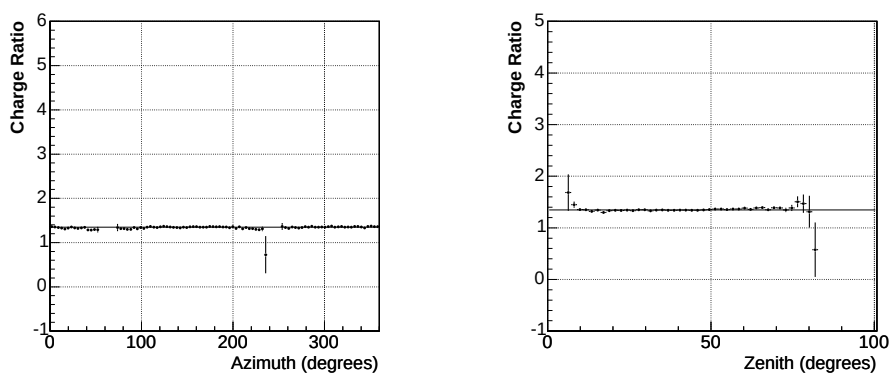

Figure 5: Charge ratio as a function of azimuth and zenith angles after combining the forward and reverse data sets.

5 Charge Ratio on Monte Carlo Samples

We repeat the studies presented in Sections 3 and 4 using Monte Carlo generated samples. The generation of these samples is described in Reference [7]. The ratio between positive and negative muons is set to 1.25. The events are reconstructed using version R1.14 of the MINOS software, the same used for real data. In Monte Carlo, the alignment of the detector is assumed to be perfect. There are a total of 2,033,996 events in the Monte Carlo sample, half of which correspond to forward field and the other half correspond to the reverse field. Table 2 shows a summary of the initial cuts applied and the number of events left after each cut.

Figures 6 and 7 show the distributions of the charge ratio as a function of momentum, ϕ, $cos(\theta)$, azimuth and zenith angles for forward and reverse field running as obtained from the Monte Carlo samples. The momentum distribution seems to have a slight dip at low momenta, but the effect is much smaller than the one observed in data. In order to see whether this is a real effect, we first remove all the cuts except the charge significance cut $(q/p)/\sigma_{q/p} > 2.5$ and finally we remove this last cut. The results are shown in Figure 8. The low momentum dip appears more significant with the charge significance cut only and then,

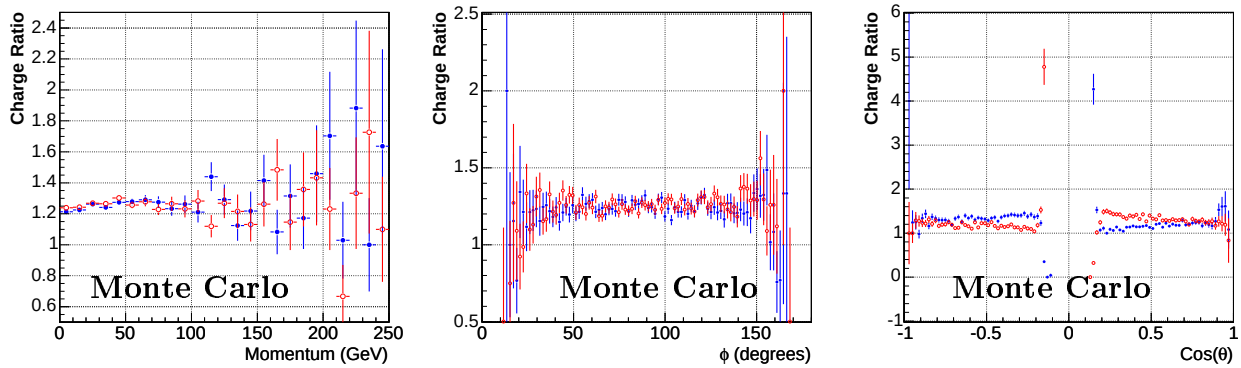

Figure 6: Charge ratio as a function of momentum, ϕ and $cos(\theta)$ for forward (full circles) and reverse (open circles) field in Monte Carlo. Compare with data in Figure 4

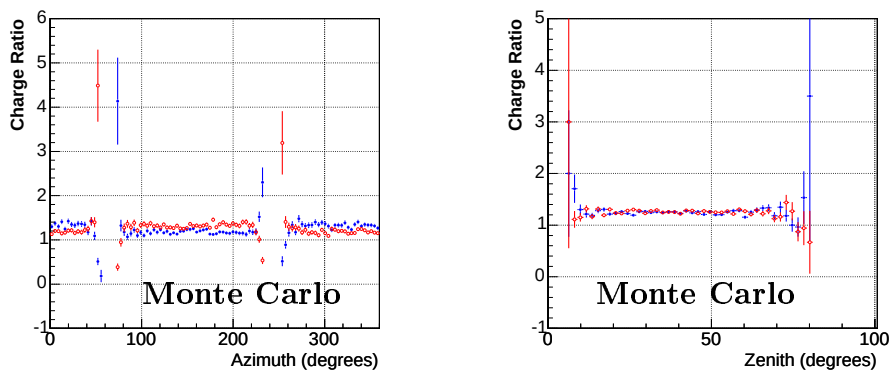

Figure 7: Charge ratio as a function of azimuth and zenith angles for forward (full circles) and reverse (open circles) field in Monte Carlo. Compare with data in Figure 5

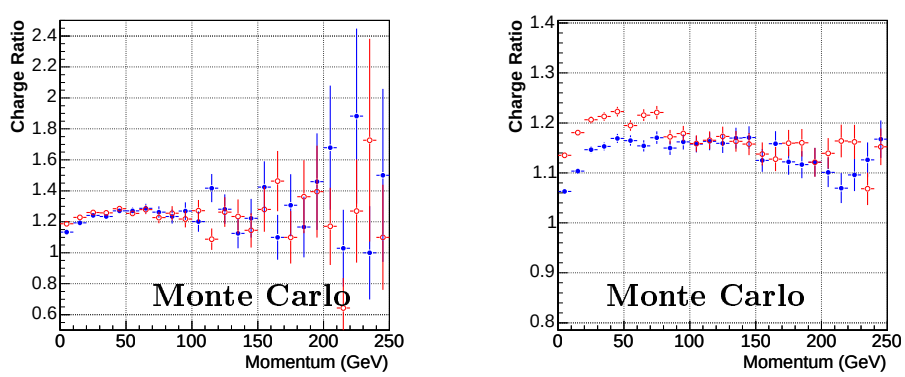

Figure 8: Charge ratio as a function of momentum for forward (full circles) and reverse (open circles) field in Monte Carlo with only the charge significance cut is applied (left) and no cuts applied (right).

Cut	Events	Fraction left (%)
no cuts	2033996	100.0
remove multiple muon events	2033815	99.99
remove demultiplexing failures	2033375	99.97
plane/digit/strip usage < 1	1995837	98.1
remove upward going	1986488	97.7
track length $> 2\ m$	1874865	92.2
plane number > 20	1508556	74.2
fit pass and $\chi^2 < 2.0$	1447146	71.1
UV asymmetry cut	1418813	69.8
fiducial cut	1417568	69.7
pulse-height and plane usage < 0.4	1416841	69.7
$(q/p)/\sigma_{q/p} > 2.5$	456498	22.4
remove stoppers	440777	21.7

Table 2: Summary of event selection criteria and the numbers of events after each cut in the Monte Carlo sample.

with all cuts removed, the dip becomes obvious as well as the split between the forward and reverse field distributions.

To further investigate the low momentum dip in the Monte Carlo results, we compare the reconstructed q/p with the true q/p, where q is the charge and p is the momentum of the track. We remove the 20 plane cut as well as the length cut (since the two are highly correlated) and then, we make a plane cut at 0, 20, 60, 100 or 150 planes. Figures 9 and 10 show the reconstructed q/p versus true q/p with each plane cut. For cuts of 0 or 20 planes, the distributions show a vertical band of mis-reconstructed events. For these events, the true q/p is very small while the reconstructed q/p seems to have random values. In terms of momenta, this means that tracks with true high momenta are reconstructed with a bias towards low momenta. Also, we note that these tracks have random reconstructed charge sign. When the reconstructed charge is random, the charge ratio is one. In a sample containing a fraction of random reconstructed charge signs, the charge ratio is lower than the true value. As the fraction of random charge events becomes dominant, the charge ratio approaches one. The charge ratio versus momentum will have a falloff (due to charge randomization) at low momenta (due to mis-reconstruction of high momentum tracks as low momentum tracks). The number of events with random charge and too low momentum is reduced as we require that the track passes through more and more planes. With 60 planes, the effect is greatly reduced and it is totally removed when 100 or more planes are required.

We have selected mis-reconstructed events with true $|q/p| < 0.25$ and reconstructed $|q/p| > 0.15$ and run the MAD event display on this sample. We find that these tracks have hits either at the start-point (vertex) or endpoint which do not belong to the track. As seen in Reference [8] this effect was initially found by scanning data events with a customized event display which takes the standard cuts of this analysis into account and selects tracks with reconstructed momentum below 5 GeV

We also find that these mis-reconstructed tracks pass through the outer regions of the

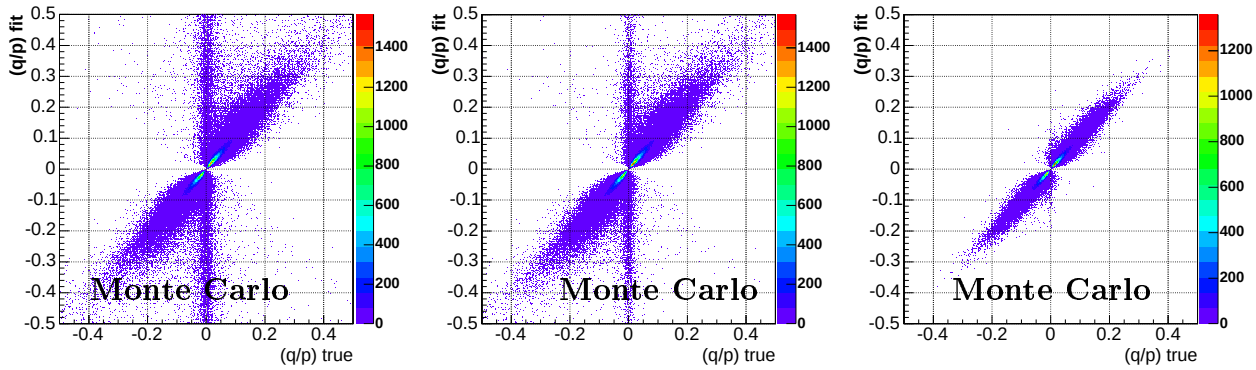

Figure 9: Reconstructed q/p versus true q/p with no plane (left), 20 plane (middle) and 60 plane (right) requirement in Monte Carlo.

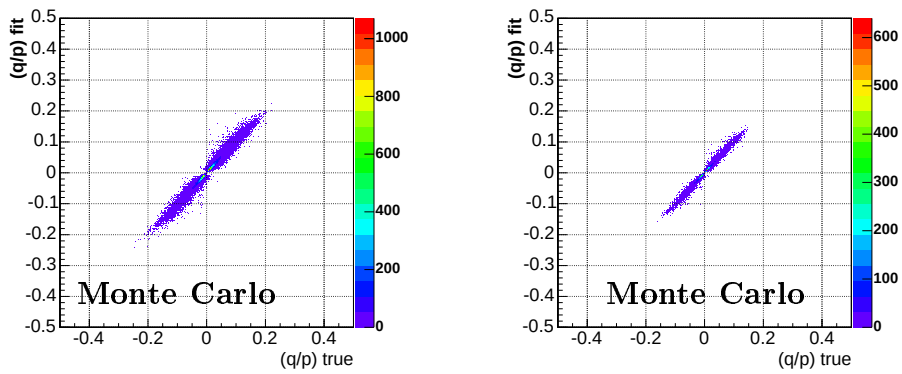

Figure 10: Reconstructed q/p versus true q/p with 100 (left), 150 plane (right) requirement in Monte Carlo.

detector. In these regions, the magnetic field is weak and the magnetic bending is comparable to the bending due to multiple scattering. These effects are discussed in Reference [6]. The conclusion is that the longer the track and the stronger the magnetic field in the regions where the track passes the detector, the more reliable is the reconstructed charge and momentum.

By comparing the distribution of the charge ratio as a function of momentum in data (Figure 4) and Monte Carlo (Figure 6), it is clear that the charge and momentum mis-reconstruction is more severe in data than in Monte Carlo. For this reason, we can not use the Monte Carlo sample to tune the cuts.

Going back to the distribution of charge ratio as a function of reconstructed momentum in real data, shown in Figure 4, we understand now the low momentum dip as an effect of mis-reconstructed charge and momentum. To remove this effect, we have to select long tracks which pass through the regions of the detector with strong magnetic field.

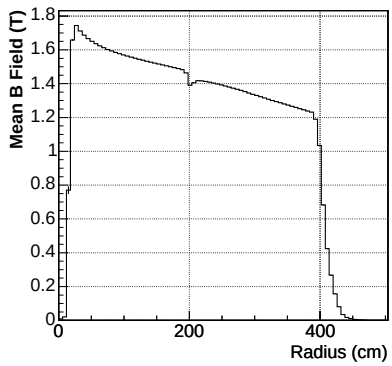

Figure 11: Mean B field in the iron planes as a function of the distance from the detector center as obtained from map 202.

6 Charge and Momentum Quality Selection

For short tracks and tracks passing through the outer regions of the detector where the magnetic field is weak and less understood, the reconstructed momentum and charge are not reliably reconstructed. The more magnetic field the tracks traverse, the more accurate the reconstructed momentum and charge. To parameterize this situation we have investigated quantities which depend on track length and magnetic field like $< B > L^2$ or $< B > L^{2.5}$ (see References [6]). Finally, we choose to construct a quantity $\int BdL$ defined as the integral along the track path of the perpendicular component of the magnetic field with respect to the track in a given point:

$$\int_{vtx}^{end} B_{perp}(r)\ dL. \tag{3}$$

where $B_{perp} = |\overrightarrow{B}(r) \times \overrightarrow{n}|$ is the component of the magnetic field perpendicular to the track direction at a given point along the track path, r is the distance from the detector center, vtx is the track vertex and end is the endpoint of the track. For the purpose of this calculation, the magnetic field is assumed to depend only on the distance from the center of the detector. We use the field map 202 to calculate the mean magnetic field as a function of the radius r. The resulting dependence $B(r)$ is shown in Figures 11. The track trajectory is approximated with a straight line between the vertex and the endpoint of the track. The integration is done numerically. For tracks that pass through the gap between the super-modules, the zero magnetic field region is removed from the integral calculation.

With the set of cuts given in Table 1 we calculate the charge ratio as a function of $\int BdL$. Figure 12 shows this dependence. The distributions corresponding to forward and reverse configurations have structures similar to the ones observed in the charge ratio versus momentum distributions. However, after combining the forward and reverse data sets, we obtain the dependence of the charge ratio versus $\int BdL$. The charge ratio approaches one for low values of $\int BdL$ where the tracks are short and pass through weak magnetic field. As $\int BdL$ increases above ≈ 12, the charge ratio reaches asymptotically a plateau value of ≈ 1.38. We identify this plateau value as the true charge ratio unaffected by randomization due to mis-reconstructed charge at low measured momenta.

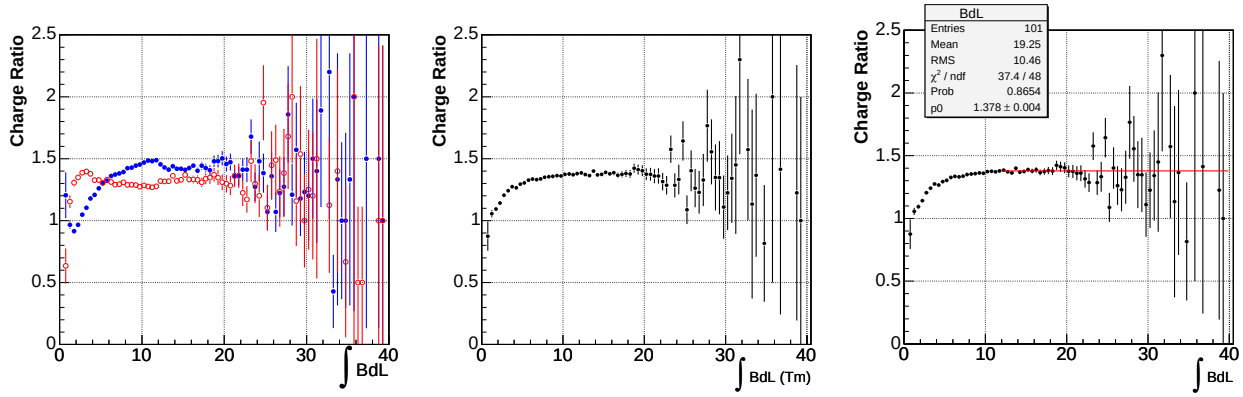

Figure 12: Charge ratio as a function of $\int BdL$ for forward and reverse data sets separately (left) and for forward and reverse configurations combined (middle). A constant fit between 12 and 40 is also shown (right).

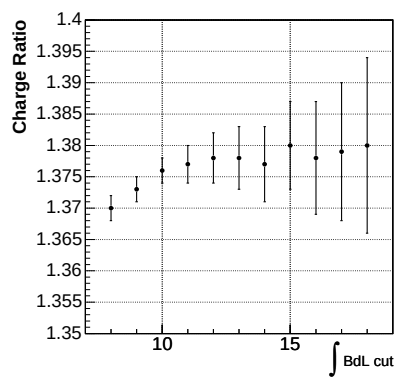

Figure 13: Charge ratio as a function of the cut value on $\int BdL$.

To precisely determine the value of $\int BdL$ where the charge ratio reaches the plateau value, we cut successively on $\int BdL$ from 8 to 18 with unit steps. At each iteration, we fit the charge ratio versus $\int BdL$ distribution with a constant function in a range starting from the corresponding cut up to 40. In Table 3 and Figure 13 we present the results of these iterative fits. The charge ratio reaches a plateau value of 1.378 ± 0.004 at $\int BdL = 12$ Tm. The fit corresponding to this cut is shown in Figure 12. It has a fit probability of 86.5%. After requiring $\int BdL = 12$ Tm we are left with a total of 627,801 events representing $\approx 3\%$ of the initial data sample.

7 Cross Checks

To investigate the validity of our result for the muon charge ratio we perform a series of cross checks. First, we study the correlations between the true q/p and the reconstructed q/p in Monte Carlo after applying the cuts in Table 1 and $\int BdL > 12$ Tm. The vertical band corresponding to events with mis-reconstructed charge and momentum is no longer present

$\int BdL$ cut	8	9	10	11	12	13	14	15	16	17	18
Central value	1.370	1.373	1.376	1.377	1.378	1.378	1.377	1.380	1.378	1.379	1.380
Error	0.002	0.002	0.002	0.003	0.004	0.005	0.006	0.007	0.009	0.011	0.014
Prob. (%)	41.1	75.6	91.3	88.2	86.5	84.9	93.8	91.9	88.7	85.9	78.8

Table 3: Results of iterative fits of the charge ratio vs.$\int BdL$ in different ranges. The central value, the error and the fit probability are shown for each cut.

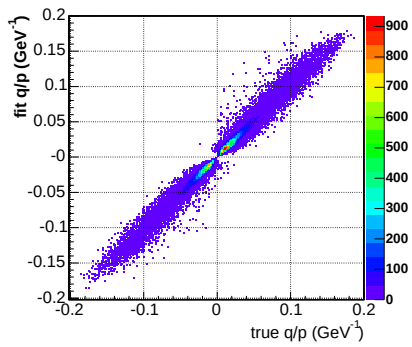

Figure 14: Reconstructed q/p versus true q/p after applying the cuts in Table 1 and $\int BdL >$ 12 Tm.

as seen in Figure 14. This a clear indication that the $\int BdL$ cut works as expected on Monte Carlo.

As a second consistency check we calculate the charge ratio as a function of reconstructed momentum after applying the cuts in Table 1 and the $\int BdL$ cut. The resulting distribution is shown in Figure 15. The low momentum dip is removed by the charge and momentum quality cut $\int BdL > 12$ Tm. The probability of a constant function fit is 32.1% and the corresponding charge ratio is 1.379±0.004, consistent with the value obtained in the previous section. However, the distribution seems to have a slight tendency to increase for high momenta. We perform a linear fit (also shown in Figure 15) and find a slope of $p_0 = 0.000281 \pm 0.000095$ and an intercept of 1.363 ± 0.006 with a fit probability of 76.7%. We divide the momentum range from zero to 250 GeV in five 50 GeV bins and fit the charge ratio in each momentum interval. The results are summarized in Table 4. We conclude that the data are consistent with either hypotheses of a constant or linear dependence.

We continue our checks by determining the charge ratio as a function of ϕ, $cos(\theta)$, azimuth and zenith angles after requiring $\int BdL > 12$ Tm. These distributions are shown in Appendix A.1 for forward and reverse, as well as for combined data sets. We note that the combined distributions are flat. The probabilities of constant function fits are excellent and the central values are consistent with 1.378 ± 0.004 for each distribution as shown in Figures 23 and 24. It is interesting to note that the structures in these distributions which were present before requiring $\int BdL > 12$ Tm are reduced, specially in the case of the charge ratio versus ϕ where the sinusoidal shape is barely visible now.

Momentum range	Charge ratio
0 - 50 GeV	1.370 ± 0.005
50 - 100 GeV	1.387 ± 0.006
100 - 150 GeV	1.389 ± 0.012
150 - 200 GeV	1.417 ± 0.025
200 - 250 GeV	1.421 ± 0.046
0 - 250 GeV	1.378 ± 0.004

Table 4: Mean charge ratio in five 50 GeV momentum bins as well as the mean value over the entire momentum range from zero to 250 GeV.

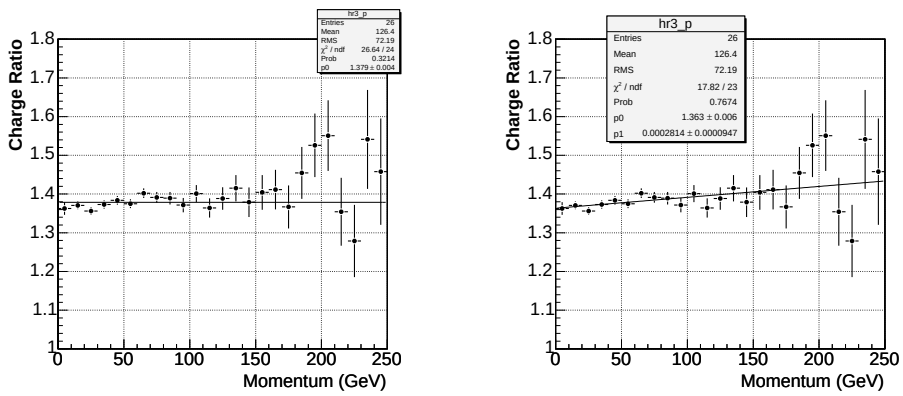

Figure 15: Charge ratio versus momentum after applying the cuts in Table 1 and the $\int BdL > 12$ cut. The distribution is fit with both a constant (left) and a linear function (right).

8 Charge Ratio versus Slant Depth

Until now we have studied the muon charge ratio as a function of momentum and direction as measured with the underground MINOS far detector. In this section we analyze the charge ratio as a function of the slant depth. For each value of the azimuth and zenith angles, the slant depth is calculated in References [9]. We use this map to obtain the slant depth for each event characterized by the azimuth and zenith angles. The map only extends from zero to 76.11° in zenith angle so, from our data sample, we select only events that correspond to this angular range. Figure 16 shows the slant depth distributions for positive and negative muons with forward field as well as the charge ratio as a function of slant depth for forward and reverse configurations. Note that the dependence of the charge ratio on field direction near 2000 m.w.e. (i.e. near vertical) is the same effect as seen in the charge ratio versus $cos(\theta)$ shown in Figure 3. Figure 17 shows the charge ratio as a function of slant depth after combining the forward and reverse data sets. We fit this distribution with both a constant and a linear function. Both fits have the same fit probability of $\approx 70\%$. The slope of the first order polynomial is only one sigma from zero. We divide the data in three slant depth bins and calculate the charge ratio in each bin. The results are summarized in Table 5. Although we confirm an increasing trend, the measurements are consistent with each other within statistical errors.

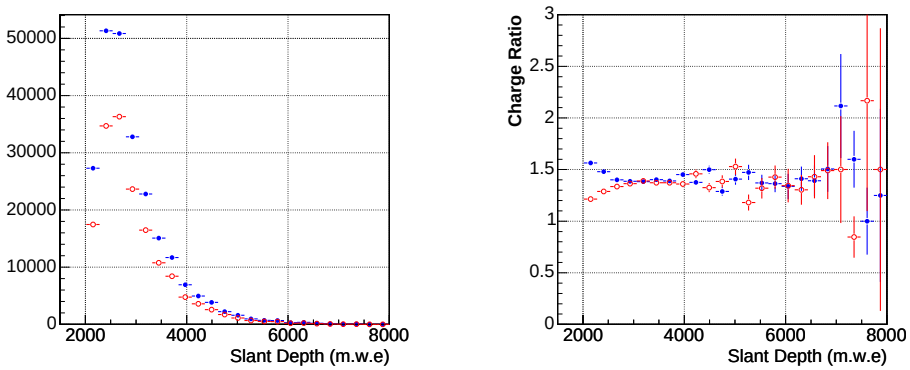

Figure 16: Distribution of slant depth for positive (full circles) and negative (open circles) muons (left) for forward field data and charge ratio as a function of slant depth for forward (full circles) and reverse (open circles) configurations (right).

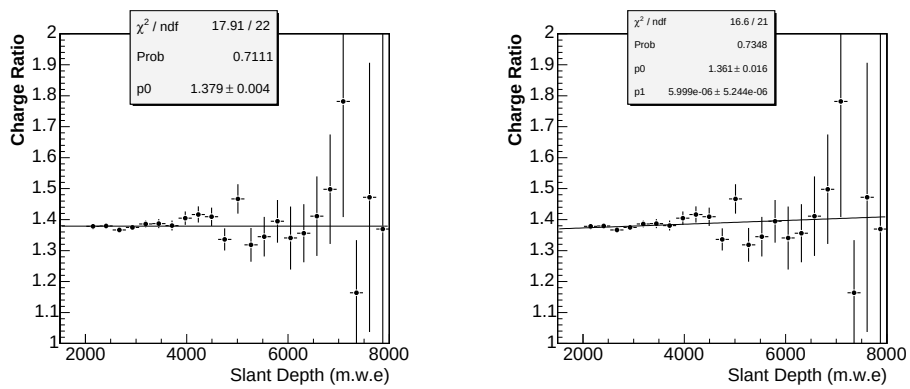

Figure 17: Charge ratio as a function of slant depth after combining the forward and reverse data sets. Constant (left) and linear (right) fits are superimposed.

9 Charge Ratio versus Surface Energy

It is of interest to determine the muon charge ratio not only as a function of the underground measured energy but as a function of the surface energy as well. To estimate the surface

Measured momentum range	Charge ratio
2000 - 2700 m.w.e.	1.375 ± 0.005
2700 - 4100 m.w.e	1.380 ± 0.005
4100 - 8000 m.w.e	1.392 ± 0.014
2000 - 8000 m.w.e.	1.379 ± 0.004

Table 5: Mean charge ratio in three slant depth bins as well as the mean value over the entire slant depth range from 2000 m.w.e. to 8000 m.w.e.

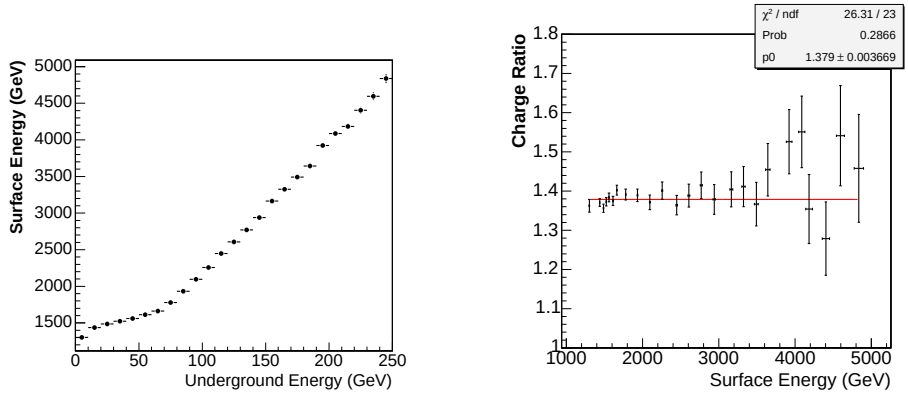

Figure 18: Mean surface energy versus underground measured energy (left) and charge ratio versus surface energy (right).

energy we use the following equation:

$$E_0 = (E + \frac{a}{b}) \times e^{bx} - \frac{a}{b}, \tag{4}$$

where E is the mean energy measured underground, E_0 is the surface energy, x is the slant depth, and the energy loss coefficients $a = 2.08 \pm 0.02 \times 10^{-3}$ GeV g^{-1} cm^2 and $b = 5.00 \pm 0.04 \times 10^{-6}$ g^{-1} cm^2 are taken from Reference [9]. Figure 18 shows the mean surface energy as a function of the underground energy and the charge ratio versus surface energy. For underground muon energies between 0 and 250 GeV, the surface energy ranges between ≈ 1.2 TeV and ≈ 5 TeV.

10 Systematic Uncertainties

Forward/Reverse Combining Procedure

As argued in Reference [5], systematic uncertainties associated with detector acceptance, curvature measurement biases and magnetic field map errors cancel out when the forward and reverse data sets are combined according to Equation (2). This statement is strongly supported by the fact that the unphysical structures that appear in the forward and reverse distributions of the charge ratio as a function of momentum, direction or slant depth are highly suppressed when we combine the forward and reverse data sets. However, we would like to quantify the degree at which this cancellation occurs. Reference [5] provides a consistency check for the applicability of Equation (2). Let $N_{F/R}^{+/-}$ be the number of positive/negative muons in the forward/reverse data set and $T_{F/R}$ the live time corresponding to the forward/reverse data set. We define the ratios $R_1 = \frac{N_F^+}{N_R^-} \times \frac{T_R}{T_F}$ and $R_1 = \frac{N_R^+}{N_F^-} \times \frac{T_F}{T_R}$. The validity of Equation (2) is equivalent with $R_1 = R_2$. A difference between R_1 and R_2 is evidence for residual systematic uncertainties.

If the muon flux were constant in time, we could calculate the live times T_F and T_R, in principle, by adding the live times of each run used in this analysis. However, we know that there are seasonal variation of the muon flux. To avoid accounting for these effects, we

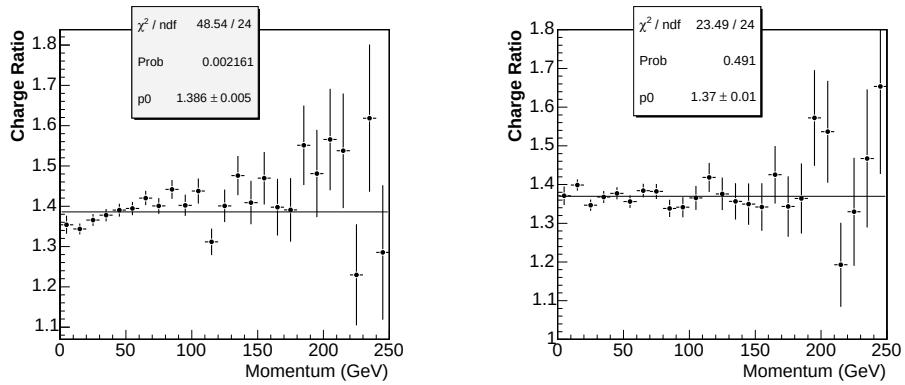

Figure 19: Distributions of R_1 (left) and R_2 (right) as a function of momentum. Constant fits to R_1 and R_2 distributions are superimposed.

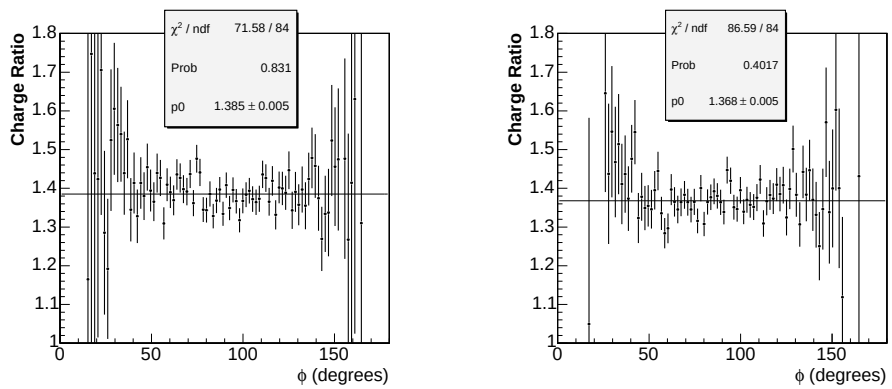

Figure 20: Distributions of R_1 (left) and R_2 (right) as a function of the angle ϕ. Constant fits to R_1 and R_2 distributions are superimposed.

use the total number of muons $N_{F/R}$ in the forward/reverse configurations as normalization factors instead of the live time $T_{F/R}$. However, this method may suffer from differences in focusing coupled with illumination effects and should be considered an upper limit on the systematic uncertainty.

In Figures 19 and 20 we show the distributions of R_1 and R_2 as a function of momentum and angle ϕ. These distributions are fit with constant functions. From the momentum distributions we obtain $R_1 = 1.370 \pm 0.005$ and $R_2 = 1.386 \pm 0.005$. As a cross check we repeat the fits for the ϕ distributions and obtain consistent results: $R_1 = 1.368 \pm 0.005$ and $R_2 = 1.385 \pm 0.005$. Clearly, there is a significant difference between R_1 and R_2. We take $(R_2 - R_1)/2 = 0.008$ as an estimate of the systematic error associated with the forward/reverse combining procedure.

Charge Significance Cut

One of the most important cuts in this analysis is the charge significance cut $(q/p)/\sigma_{q/p} > 2.5$ which together with the $\int BdL$ cut ensures a selection of events with accurately reconstructed charge and momentum. Figure 21 shows the distribution of the muon charge ratio as a

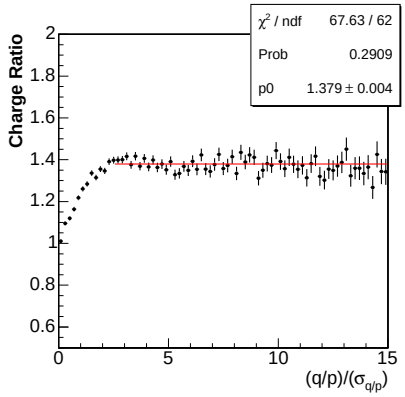

Figure 21: Charge ratio versus charge significance $(q/p)/\sigma_{q/p}$.

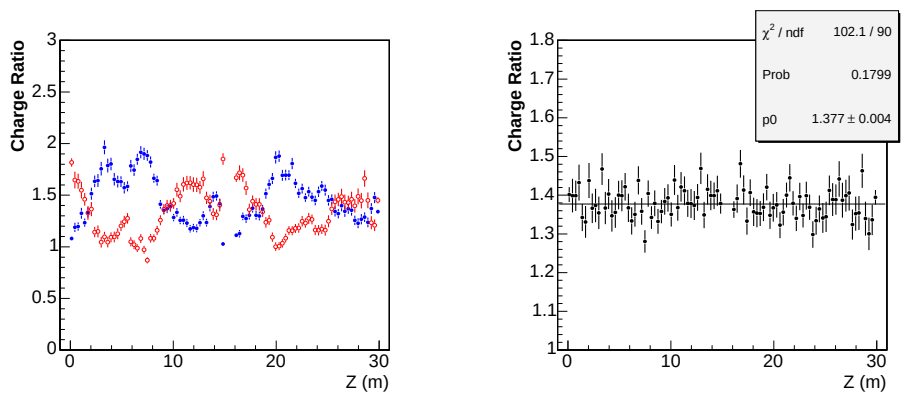

Figure 22: Charge ratio versus the Z position of the track vertex for forward (full circles) and reverse (open circles) configurations (left) as well as the combined case (right).

function of $(q/p)/\sigma_{q/p}$. The charge ratio approaches one as $(q/p)/\sigma_{q/p}$ tends to zero. This simply means that the charge identification is totally randomized when $(q/p)/\sigma_{q/p} = 0$. As the charge significance increases, the charge ratio increases as expected and it reaches a plateau value when $(q/p)/\sigma_{q/p} > 2.5$. In our determination of the charge ratio we only selected events with $(q/p)/\sigma_{q/p} > 2.5$. To study the systematic error associated with this requirement we follow the procedure used in References [1]. We fit the charge ratio versus $(q/p)/\sigma_{q/p}$ for $(q/p)/\sigma_{q/p} > 2.5$ with a constant function as show in Figure 21. The fit result is 1.379 ± 0.004. We take the error on this measurement as the systematic uncertainty associated with the the charge significance cut.

$\int BdL$ Cut

We saw that in order to select events with correctly reconstructed charge and momentum we require that $\int BdL > 12$. We take the largest deviation between the charge ratio with $\int BdL > 12$ and the charge ratio with any higher cut. From Table 3 we find that the largest deviation is 0.002 which is our conservative estimate of the systematic uncertainty associated with the $\int BdL$ cut.

Summary of Systematic Uncertainties

We calculate the total systematic error by adding in quadrature the individual errors described above. With this, the total systematic uncertainty on the charge ratio is 0.009.

11 Further Consistency Checks

We repeat the measurement of the charge ratio in three subsample: tracks contained in super-module 1, tracks contained in super-module 2 and track that pass through both super-modules. The resulting values of the charge ratio as obtained by fitting the charge ratio versus momentum distributions with constant functions are 1.380 ± 0.006, 1.376 ± 0.006 and 1.377 ± 0.009, respectively. These values are statistically consistent with the value obtained from the entire data sample, showing that there are no systematic effects associated with differences between the two super-modules.

In Figure 22 we plot the charge ratio versus the Z position of the track vertex for both forward and reverse cases as well as for the combined case. Large variations of the charge ratio are observed for both forward and reverse configurations, but in the combined case, the charge ratio is flat as expected.

We combine the first forward field data set with the first half of the reverse field data set and obtain a charge ratio of 1.378 ± 0.005. Then we combine the second half of the reverse field data set with the second forward field and obtain 1.377 ± 0.006. These results are consistent with the value obtained from the entire data sample, showing that there are no systematic effects associated with specific periods during data taking.

12 Conclusions

We have analyzed the atmospheric muon charge ratio using data collected with the MINOS far detector. We obtain a value of $1.378 \pm 0.004(stat.) \pm 0.009(syst.)$ for an underground energy range from zero to 250 GeV corresponding to an estimated surface energy range from ≈ 1.2 TeV to ≈ 5 TeV.

A Appendix

A.1 Charge Ratio after the $\int BdL > 12$ Cut

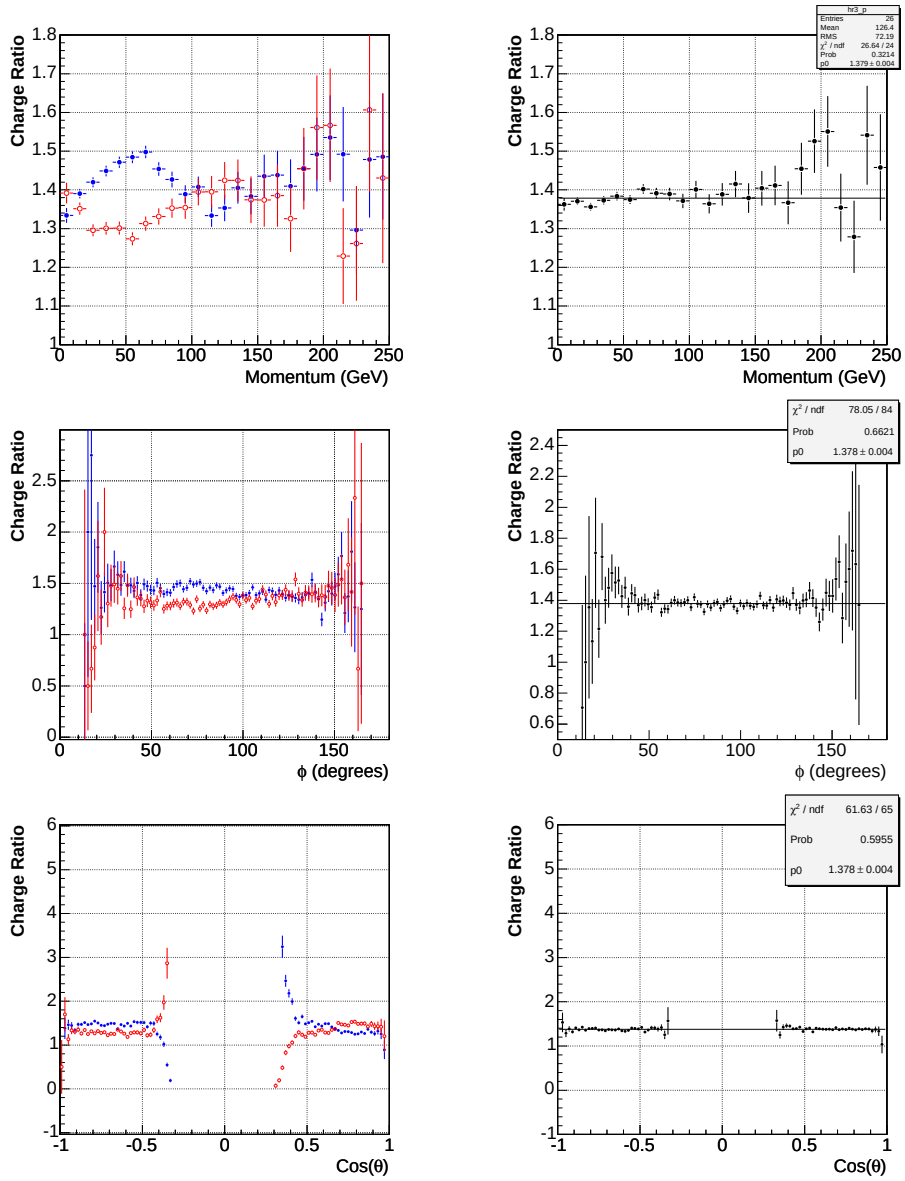

Figure 23: Charge ratio versus momentum (top), ϕ (middle) and $cos(\theta)$ (bottom) for forward (full circles) and reverse (open circles) on the left hand side and combined on the right hand side.

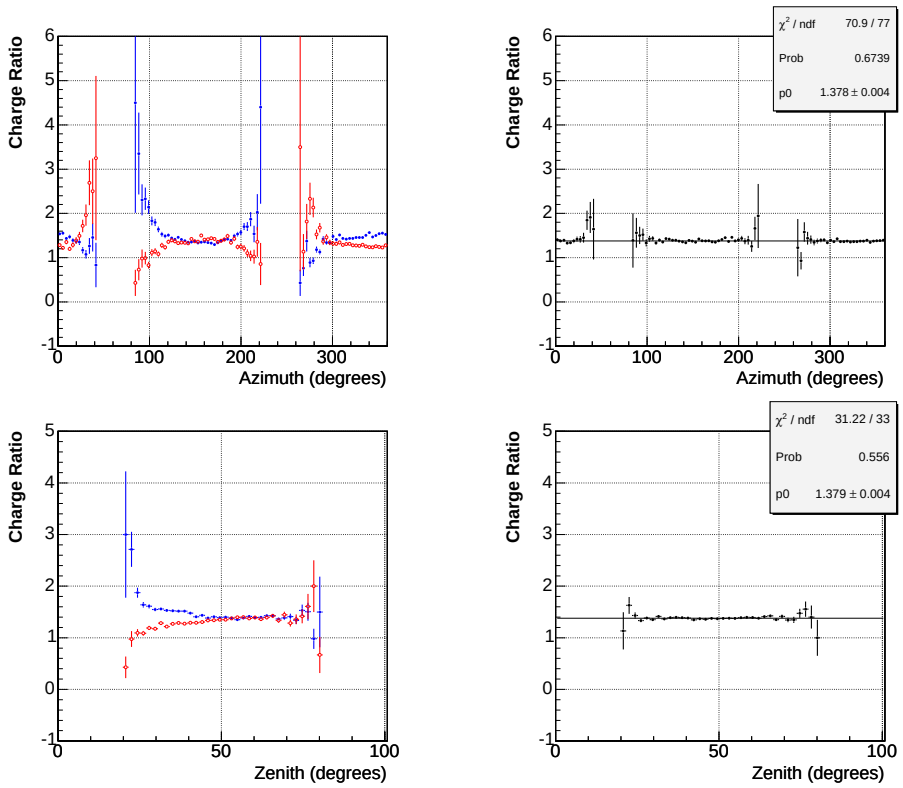

Figure 24: Charge ratio versus azimuth (top) and zenith (bottom) for forward (full circles) and reverse (open circles) on the left hand side and combined on the right hand side.

References

[1] S. L. Mufson, B. J. Rebel, "Cosmic Muon Physics with the MINOS Far Detector", NUMI Note 1099.

[2] B. Rebel, "Neutrino-Induced Muons in the MINOS Far Detector", Ph.D Thesis, Indiana University, 2004.

[3] E. Beall, "Cosmic Ray Muon Charge Ratio in the MINOS Far Detector", Ph.D Thesis, University of Minnesota, 2005.

[4] P. Schreiner, V. Frohne, M. Goodman, T. Fields, "MINOS Far Detector Acceptance Study for Understanding Aspects of the Mufson Effect", NUMI note 1049.

[5] T. Fields, "Systematic Errors in the Cosmic Muon Charge Ratio Measurement", NUMI note 1483.

[6] T. Fields, "Maximum Detectable Momentum in the MINOS Far Detector", NUMI note 1511.

[7] `http://www.hep.phy.cam.ac.uk/minos/group/mc/mc_nov04_map201.html`

[8] `http://www.hep.anl.gov/jurgenr/Midad4ANL.ppt`

[9] S. Kasahara, " A Study of Cosmic Ray Composition in the Knee Region using Multiple Muon Events in the Soudan 2 Detector", Ph.D Thesis, University of Minnesota, 1997 `http://webusers.physics.umn.edu/ schubert/far/s2rock/`